Surface Charge- and Space-Dependent Transport of Proteins in Crowded Environments of Nanotailored Posts

Chang Kyoung Choi,[†] Jason D. Fowlkes,[‡] Scott T. Retterer,[‡,§] Piro Siuti,[§,⊥] Sukanya Iyer,[§,⊥] and Mitchel J. Doktycz[‡,§,⊥,*]

[†]Mechanical Engineering—Engineering Mechanics, Michigan Technological University, Houghton, Michigan 49931-1295, [‡]Center for Nanoscale Materials Sciences, and [§]Biosciences Division, Oak Ridge National Laboratory, Oak Ridge, Tennessee 37831, and [⊥]Graduate Program in Genome Science and Technology, University of Tennessee, Knoxville, Tennessee 37996

ABSTRACT The reaction and diffusion of molecules across barriers and through crowded environments is integral to biological system function and to separation technologies. Ordered, microfabricated post arrays are a promising route to creating synthetic barriers with controlled chemical and physical characteristics. They can be used to create crowded environments, to mimic aspects of cellular membranes, and to serve as engineered replacements of polymer-based separation media. Here, the translational diffusion of fluorescein isothiocyante and various forms of green fluorescent protein (GFP), including "supercharged" variants, are examined in a silicon-based post array environment. The technique of fluorescence recovery after photobleaching (FRAP) is combined with analytical approximations and numerical simulations to assess the relative effects of reaction and diffusion on molecular transport, respectively. FRAP experiments were conducted for 64 different cases where the molecular species, the density of the posts, and the chemical surface charge of the posts were varied. In all cases, the dense packing of the posts hindered the diffusive transport of the fluorescent species. The supercharged GFPs strongly interacted with oppositely charged surfaces. With similar molecular and surface charges, transport is primarily limited by hindered diffusion. For conventional, enhanced GFP in a positively charged surface environment, transport was limited by the coupled action of hindered diffusion and surface interaction with the posts. Quantification of the size-, space-, time-, and charge-dependent translational diffusion in the post array environments can provide insight into natural processes and guide the design and development of selective membrane systems.

KEYWORDS: diffusive transport · reaction—diffusion · post array · nanopost · fluorescence recovery after photobleaching (FRAP)

Biomolecular transport in cellular environments occurs in crowded surroundings where molecular reactivity and diffusion can be significantly altered when compared to dilute solution conditions. These changes in physical parameters are integral to biological function and can lead to self-organization, controlled reactivity, and defined flux through molecular networks.[1,2] Gaining the ability to replicate this functionality will be key for applying biological design principles to synthetic constructs. By the prescribed design of spatially restricted environments, micro- and nanofabrication techniques can facilitate these efforts. Physical obstacles and pore structures with precisely controlled locations and dimensions are routinely fabricated and have been used to differentially affect the transport of biomolecules. For example, sieves,[3,4] sifters,[5] nanochannels,[6,7] and nanopores[8] can be constructed and have been applied for high-resolution separations and selective isolations. The sorting of proteins and nucleic acids,[9] the controlled delivery of pharmaceuticals, and the development of diagnostic devices[3−6,9,10] have been demonstrated. Controlled fabrication facilitates the design and modeling of separation systems, while the robust mechanical properties and functional integration capabilities of silicon-based structures facilitate the production of useful devices.

Micro- and nanofabricated structures can also be arranged to form small volume reaction containers that mimic other aspects of biological cells.[11−13] Natural cells use a membrane to encase the cell's contents[14] and to regulate transport in and out of cellular and subcellular domains.[15] Natural membranes can be specialized and provide a host of different functions. Advances in fabrication technology allow integration of chemical and physical features across the nano- and microscales that can provide related functionality. For example, the defined volume and controlled flux afforded by natural membranes can be replicated with synthetic structures to create synthetic cells or cell mimics.[16−19] Developments related to the encasing membrane have focused on refining size selectivity and are advancing toward adding chemically selective functionality.[11,20−23] Adding dynamic properties to such membranes and separation systems is also possible.[22,24,25] The refinement of multiscale structures with different

*Address correspondence to doktyczmj@ornl.gov.

Received for review December 15, 2009 and accepted May 24, 2010.

Published online June 1, 2010.
10.1021/nn901831q

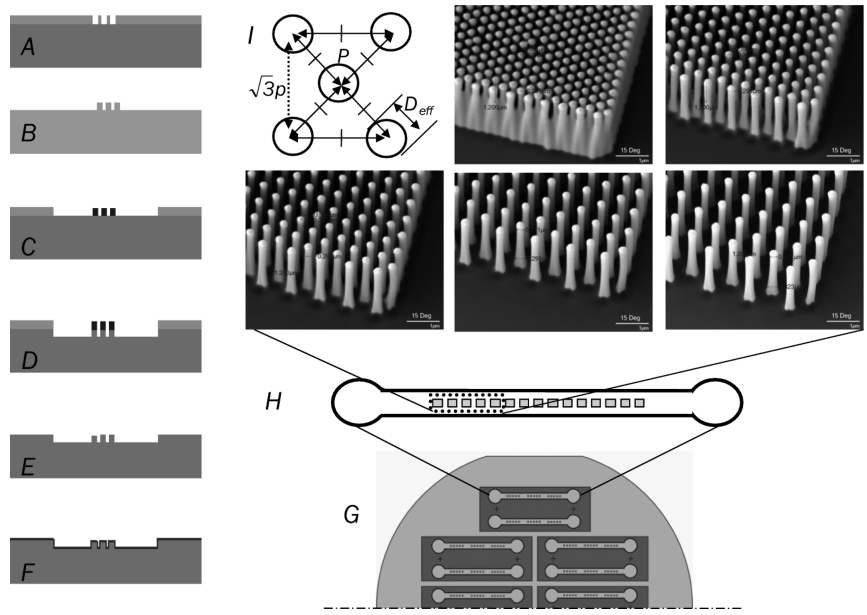

Figure 1. Schematic of postarray structures. (A−F) Diagram of the microfabrication process viewed in cross section; (A) post pattern is defined in photoresist using electron beam lithography; (B) Cr evaporation and lift-off Cr; (C) photolithographic definition of the microfluidic channels; (D) deep RIE process is applied using Oxford Plasmalab 100 to define the microchannels; (E) photoresist and Cr are chemically removed; (F) silicon dioxide coating is applied using PECVD. (G) Sketch of half of the wafer which consists of 4 fluidic devices, each containing a pair of channels. (H) Sketch of a microchannel device with the embedded post arrays and electron micrographs of the post arrays of 200 nm nominal diameter posts, where their pitches are 400, 500, 600, 700, and 800 nm. (I) Sketch of post distribution, diameter, and pitch.

physicochemical features will be essential to realizing biological design principles.

Whether crossing a cellular membrane or transporting across a cell, diffusion can play a crucial role in the movement of molecular species. Being a passive process, diffusion does not require the input of energy yet can be an effective means for transport and mixing in small volumes such as the cell.[26,27] When considering the diffusion of intracellular molecules/particles in a complex biological environment, molecular transport is generally classified into two categories; "Fickian" type diffusion (D_o) and/or hindered diffusion (D_h). Hindered diffusion results when molecular crowding, immobile molecules/barriers, and/or molecular binding interactions effectively reduce the magnitude of the diffusion coefficient below the value predicted by the Stokes−Einstein equation. Interpreting hindered diffusion in the complex environment of the cell can be a difficult task. Further, particle hydrodynamics can change significantly when the diffusing species approaches other objects, such as in the crowded molecular environment of a cell.[28−32] In general, the intracellular diffusion of proteins, vesicles, and/or molecules is hindered (see Figure S1 in Supporting Information) and integral to the operation of cellular processes.[33] Replicating these characteristics in synthetic systems may reveal a deeper understanding of biological processes as well as a means for exploiting such environments for applied uses.

To gain a better understanding of reaction and diffusion within crowded synthetic material systems, etched silicon post structures of different diameter, periodic spacing, and surface functionality were prepared and investigated for their ability to hinder diffusion of molecular species of different sizes and charges. The post structures are mechanically stable, and the diameters of the posts as well as their location can be precisely controlled. Additionally, the post diameters can be further tailored using plasma-enhanced chemical vapor deposition (PECVD)[34] and the chemical characteristics of the post array surfaces modified through silane chemistry. Hindered diffusion of enhanced and "supercharged" GFP as well as the small molecule fluorescein isothiocyanate (FITC) in a silicon-based post array environment was quantified using fluorescence recovery after photobleaching (FRAP).[35] FRAP is a powerful method for characterizing diffusion in a microscale region-of-interest (ROI) and for measuring diffusive transport rates in complex nanoscale environments. Experimental results are compared with the results of finite difference simulations to predict diffusion and analytical approximations to quantify binding interactions with the posts. This combination of quantitative measurement and computational simulation ultimately enables the interpretation of how molecular characteristics and device design parameters affect mass transport in synthetically crowded environments.

RESULTS AND DISCUSSION

Physical Characteristics of the Post Arrays. The etched post arrays, shown in Figure 1, were prepared at a variety of diameters and pitches so as to evaluate the effects of

TABLE 1. Diameters of Posts and Experimental Matrix[a]

case	d_0 [nm]	d_t [nm]	d_b [nm]	d_{eff} [nm]	eGFP and FITC	−30GFP	+36GFP
PA I_1	50	217.0	417.0	297.0	x		
PA I_2	100	303.8	386.0	336.7	x		
PA I_3	200	319.7	411.5	356.4	x		
PA I_4,5	200	332.2	472.0	388.1		x	x
PA II_1	50	215.0	426.0	299.4	x		
PA II_2	100	247.0	464.0	333.8	x		
PA II_3	200	363.3	510.3	422.1	x		
PA II_4	200	276.8	310.7	290.4		x	
PA II_5	200	337.5	487.2	397.4			x

[a]Post arrays (PA) I and II represent cell mimic membranes coated with silicon dioxide and 3-aminopropyltrimethoxysilane, respectively. d_o, d_t, d_b, and d_{eff} represent the nominal diameters of the posts, the diameters at the top of posts, the diameters of the bottom of posts, and the effective diameter considering appropriate geometric conditions, respectively.

surface area and volume on diffusive transport. Increases in surface area and occupied volume should enhance the influence of adsorption and molecular exclusion on transport processes, respectively. To facilitate experimental measurements, different pitches of a particular post diameter were prepared within a single 200 μm wide microfluidic channel. This allowed rapid assessment of post geometry while minimizing differences in experimental conditions. A single wafer contained 16 identical fluidic devices. Different post diameters were prepared using a separate set of masks and wafers due to changes in etching conditions required to prepare high aspect ratio posts of different diameters. While there was a uniform size distribution of diameters (less than 5.6% variation) and pitches for posts observed in a single wafer, some wafer to wafer variation was observed. To ensure accurate interpretation of experimental results, the post diameters were measured by SEM before and after experiments. The gap (pitch) between posts was also checked by SEM and with polystyrene fluorescent particles using microfluidics (Figure S2 in Supporting Information).

Table 1 displays the nominal and measured values for the different post geometries used in the experiments described below. Post arrays (PA) I and II represent post arrays coated with silicon dioxide (SiO_2) or further coated with 3-aminopropyltrimethoxysilane (3-APTMS), respectively. Thus PA I structures have negatively charged surfaces, while PA II structures have positively charged surfaces at neutral pH. The d_0 is the nominal, designed diameter of the posts and was either 50, 100, or 200 nm. After etching and oxide deposition, the post diameters were measured and d_t and d_b are the average top and bottom diameters of the posts, respectively; d_{eff} is the average of these values and was used as the effective diameter for simulations. The 50 and 100 nm nominal diameter posts were arranged at four different pitches of 400, 500, 600, and 700 nm. The 200 nm diameter posts were arranged at pitches of 500, 600, 700, and 800 nm. This resulted in 12 different post densities with two different surface characteristics.

The resulting density of the posts ranged from 7.8 posts/μm^2 for the most crowded environment to 1.8 posts/μm^2 for the least crowded environment. This corresponds to an occupied cross-sectional surface area (OCSA) of 65 to 12%. For reference, the values for crowding in bacterial cells can range from 20 to 30%.[36] Figure 2a displays the range of OCSAs for the structures

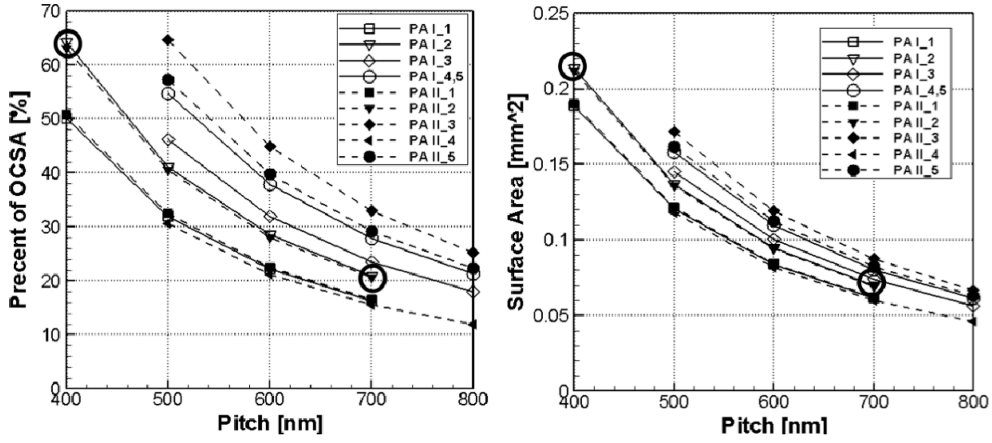

(a) OCSA (b) Surface area

Figure 2. Physical dimensions: (a) percent of estimated OCSA and (b) cylindrical SAs of posts in the post array (100 × 100 μm^2).

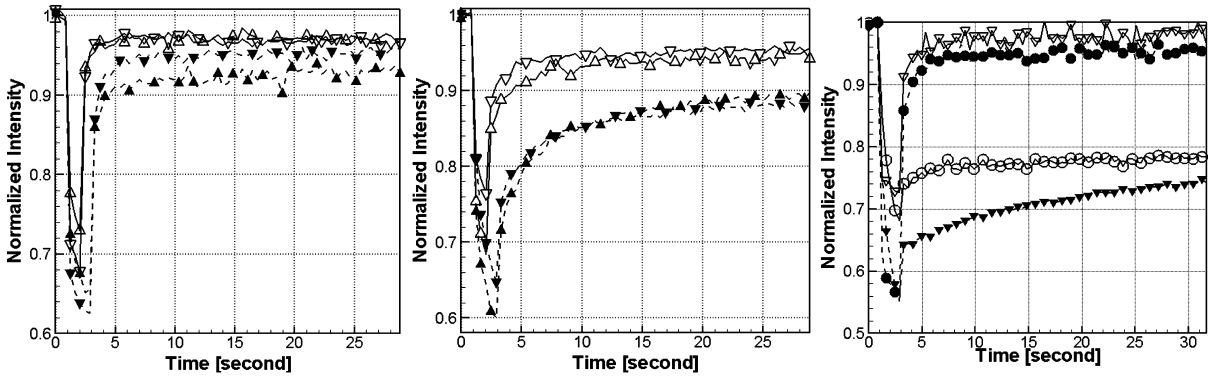

Figure 3. Qualitative assessment of molecular diffusion in post array structures. (a) Selected exemplary FRAP data of FITC for extreme conditions of OCSA (∇ on SiO_2 with OCSA of 20.9%, Δ on SiO_2 with OCSA of 64.3%, ▼ on 3-APTMS with OCSA of 20.6%,▲ on 3-APTMS with OCSA of 63.2%). (b) FRAP curves of eGFP for extreme conditions of SA (∇ on SiO_2 with SA of 0.07 mm^2, ▲ on SiO_2 with SA of 0.214 mm^2, ▼ on 3-APTMS with OCSA of SA of 0.07 mm^2, ▲ on 3-APTMS with SA of 0.212 mm^2). (c) Supercharged proteins on oppositely charged surfaces (○ +36GFP on SiO_2, ∇ −30GFP on SiO_2, ● +36GFP on 3-APTMS, ▼ −30GFP on 3-APTMS). Note that filled symbols represent 3-APTMS-coated surfaces, while empty symbols represent silicon dioxide surfaces. For clarity, symbols represent every fifth data point.

that were evaluated. Figure 2b displays the estimated surface area (SA) that results from the post patterns. The posts lead to surface areas on the order of 6−21 times (for larger and smaller pitches, respectively) greater than the planar surface (100 μm × 100 μm) from which they were prepared. The gap spacing between the posts ranged from approximately 60 to 430 nm.

Qualitative Assessment of Molecular Diffusion in Post Array Structures. The diffusion of relatively small and large molecules was examined by FRAP in these structures, as summarized in Table 1. Three different variants of GFP were considered in this study. In addition to enhanced green fluorescence protein (eGFP), which has a net charge of −7, supercharged GFPs with a net charge of −30 and +36 were also evaluated.[37] These proteins should accentuate potential electrostatic interactions with the post structures. FITC was used as a small molecule comparison. Figure 3 shows selected FRAP recovery data for FITC (Figure 3a), eGFP (Figure 3b), and the supercharged GFP variants (Figure 3c) on SiO_2 and 3-APTMS surfaces. The post array environments used for these experiments correspond to fairly large differences in post array density and are the circled values shown in Figure 2. These conditions represent extreme values of OCSA and SA and allow for qualitative assessments of the effects of OCSA and SA on molecular diffusion. The FRAP experiment consists of three primary steps. A brief prebleaching step is used for subsequent normalization of the fluorescent signal and utilizes low laser power to avoid unnecessary photobleaching. The bleaching step uses maximal laser intensity and is used to bleach the fluorophore present in a defined region of interest. The postbleaching (recovery) regime uses the same reduced power as the prebleaching step and is monitored at appropriate time intervals until the fluorescent signal has recovered. For the experiments reported here, the maximum frame acquisition rate of 1 kHz was used for data collection, resulting in the minimum time interval of 406 ms between data points. Each data point is normalized by dividing its intensity with the average intensity measured during the prebleaching process. The shape of the curve in the recovery region is indicative of the diffusion rate.

In general, a maximum fluorescent bleaching of only 25 to 50% was observed in the post array environments. This can be attributed partially to the diffusion of mobile fluorophore back into the region of interest during the bleaching process. The reduced bleaching in the post array environment is also likely due to optical interferences with the subwavelength patterns of the post array structures. Nevertheless, sufficient bleaching was obtained to allow for interpretation of diffusion rates. In many cases, incomplete recovery of fluorescence after the photobleaching step was also observed. The majority of the FRAP curves shown in Figure 3 show on the order of 89−96% recovery of the fluorescent signal, while the experiments involving supercharged GFP, in environments with oppositely charged surfaces (Figure 3c), show even less recovery (on the order of 75−78%). The fraction of fluorescence signal that does not recover likely corresponds to immobilized fluorophore. This immobilized fluorophore may be bound to the post array surface and remains bound after bleaching. Alternatively, mobile fluorophore that becomes bleached may become immobilized.

As expected, the diffusion-based recovery of the smaller FITC molecules (hydrodynamic radius = 0.54 nm) is faster than the larger GFP molecules. Shown in Figure 3a are FRAP data for FITC in post array environments for two extreme cases of occupied area. The recovery portion of the curve appears to be largely insensitive to the post array density. Also shown are

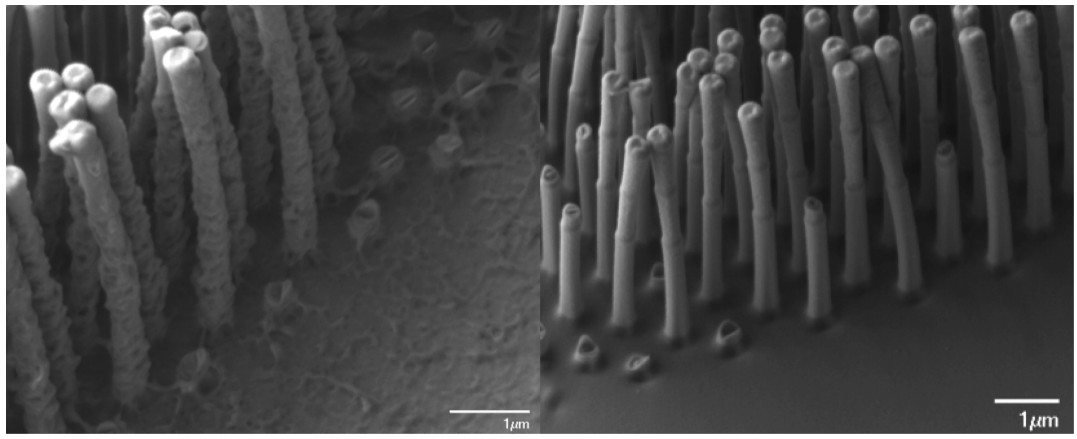

Figure 4. SEM images of post arrays after experiment for (a) −30GFP and (b) +36GFP on the 3-APTMS surface after sonicating the post arrays in deionized water.

fluorescence recovery data for FITC in array environments with similar occupied areas but different surface charges. For the positively charged 3-APTMS surface, the fraction of immobile fluorophore is larger than that of the native SiO_2 surfaces. This is consistent with an electrostatic interaction between the negatively charged FITC and the positively charged silane-treated surface.

FRAP recovery data for eGFP are shown in Figure 3b. The post geometries and surface charge environments are similar to those described for the FITC experiments. As with the FITC recovery curves, there is, at most, only a mild affect of occupied area or surface area on the fluorescence recovery data. The eGFP does show a gradual fluorescence recovery when compared to FITC, indicating slower diffusional transport. The eGFP has a net charge of −7, and the fluorescence recovery is even more gradual for surfaces coated with 3-APTMS when compared to the native silicon dioxide surfaces. This is consistent with electrostatic interaction between the molecule and the positively charged surface and the possibility that binding interactions further affect the transport process. The fraction of immobile fluorescence signal also increases with complementary charges, further supporting the observation of interactions between the molecule and the surface.

The importance of charge−charge interactions in affecting transport is further exemplified in the FRAP experiments that involve the supercharged GFPs. Figure 3c shows selected FRAP experimental data for supercharged proteins (+36GFP and −30GFP) on the SiO_2 and the 3-APTMS surfaces with similar surface areas and volume crowding. For supercharged GFPs with the same charge as on the surface, there is a relatively fast recovery when compared to supercharged GFPs with charges opposite to that of the surface. For situations with complementary charges, there is a substantial immobile fraction when compared to the supercharged proteins with like charges to the surface or to situations involving FITC or eGFP. This can be attributed to the significant surface charge of the supercharged molecules. The strong electrostatic attraction between the supercharged protein and the oppositely charged surface is supported by postexperiment electron micrographs of the surfaces, as shown in Figure 4. The native oxide surfaces show significant surface coatings when compared to the positively charged post surfaces after exposure to the negatively supercharged GFPs.

Quantitative Assessment of Reaction and Diffusion in Post Array Structures. Figure 5 shows a model fluorescence recovery curve that is representative of a typical curve observed in this work. Select parameters that can be derived from the curve are superimposed over the

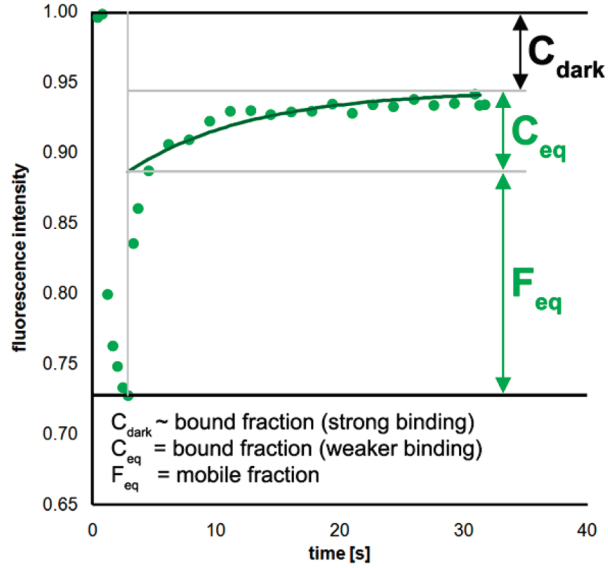

Figure 5. Model representation of a typical fluorescence recovery curve. A relatively strong binding interaction can reduce the post recovery, FRAP intensity below the prebleach intensity due to a bound and bleached molecular fraction (C_{dark}). The rate of fluorescence recovery was found to be dictated by a relatively weaker binding interaction. Extrapolation of this bound fraction (C_{eq}) could be estimated by fitting the portion of the recovery curve affected by binding to a binding model. F_{eq} represents the mobile fraction of molecules in equilibrium with this bound state.

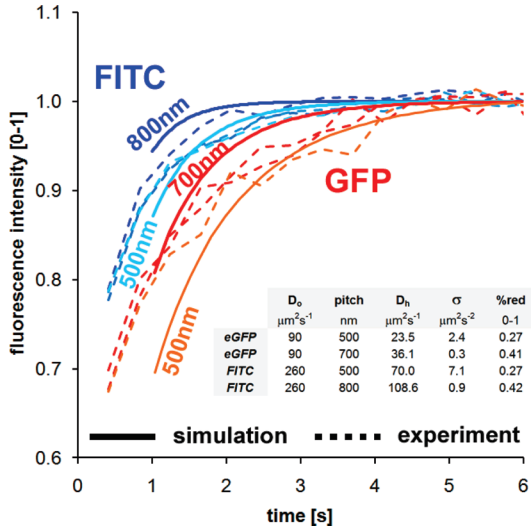

	D_o $\mu m^2 s^{-1}$	pitch nm	D_h $\mu m^2 s^{-1}$	σ $\mu m^2 s^{-2}$	%red 0-1
eGFP	90	500	23.5	2.4	0.27
eGFP	90	700	36.1	0.3	0.41
FITC	260	500	70.0	7.1	0.27
FITC	260	800	108.6	0.9	0.42

Figure 6. Diffusion-dependent fluorescence recovery *vs* post pitch for FITC and eGFP. Experimental data are shown as the hatched lines, and simulated data are shown as the solid curves. The reduction in the diffusion coefficient (%red) due to the occupied volume by posts is shown superimposed over the figure in tabular form. The value of the hindered diffusion coefficient (D_h) and the standard deviation (σ) in this value are also shown. The FRAP simulations were conducted using the combined approach of a random walk, particle tracking simulation, and a finite difference solver.

schematic and described in detail in the Methods section. The treatment described by Sprague *et al.*[38] was used in the following analyses. For the described FRAP experiments, a tightly bound fraction was observed in specific cases (opposite surface and molecule polarities) that did not recover in response to photobleaching. This bound fraction is labeled as C_{dark} in the figure. However, the *rate* of fluorescence recovery was found to be governed by a much weaker binding state that did recover over the course of a typical FRAP experiment ($t \sim 60$ s). The best fit of the time-dependent fluorescence intensity to this region was used to extrapolate back to $t = 0$ s, the termination of photobleaching, in order to determine the fraction of fluorescence due to bound (C_{eq}) and unbound (F_{eq}) molecules within the bleach ROI. From these fits, a value for k_{off}, the off-rate for the binding interaction, could be determined.

Pure Diffusion Dominant Behavior. The particle tracking simulation, coupled with the finite difference method, made it possible to estimate the reduction in the diffusion coefficient from D_o to D_h that occurs due to changes in molecular species and post array dimensions. Figure 6 shows a cluster of experimental FRAP curves (hatched lines) for both FITC (blue traces) and eGFP (red traces) as well as for a host of array dimensions. In cases where the post array dimensions were changed, the post diameter was fixed at $d_{eff} = 356$ nm, while the post spacing was changed. Finite difference simulation results are shown as the solid curves with the post pitch for each experiment labeled on the figure.

Fluorescence recovery profiles were found to be mostly insensitive to changes in pitch for the pitch range of 500−800 nm. For example, Figure 6 shows that fluorescence recovery curves actually overlap in places for experiments conducted at the extreme values of pitch range (*i.e.*, 500 and 800 nm), due to the noise in the fluorescence recovery curves. This result was confirmed by finite difference simulations of diffusion that predicted the observed difference in fluorescence recovery for extremes in post pitch. Thus, the results presented in Figure 6 suggest that pure diffusion dominant behavior dictated fluorescence recovery.

The superimposed table within Figure 6 summarizes the estimated change in D_h derived from the simulations. As expected, GFP diffusion is slower than that observed for FITC, in accord with the increase in molecular size. Regardless of the type of molecular species, diffusion was reduced by 73% for a post pitch of 500 nm and by ~59% for a pitch of 800 nm. In the case of eGFP, $D_h = 23$ μm²/s (pitch = 500 nm) and $D_h = 36$ μm²/s (pitch = 800 nm) are reduced from the *in vitro* value of $D_o = 87$ μm²/s in water. These values are consistent with those reported for GFP in the biological cell.[39] This observation implies that posts of these dimensions could serve to replicate diffusive behavior in cell-like environments, independent of the containment volume.

Reaction Dominant Behavior. For supercharged GFP variant diffusion in a like surface charge environment, the majority of fluorescence recovery can be attributed to mobile protein as judged by the high value observed for F_{eq} (Table 2). Figure 7 shows the rapid rate of recovery observed for both the (+36)GFP/(+)3-APTMS and (−30)GFP/(−)SiO_2 cases. Further, nearly full fluorescence recovery is observed, and interactions with the posts do not significantly alter the recovery. (There is a weak binding interaction observed for all GFPs tested,

TABLE 2. Binding Parameters Obtained from Numerical Simulations[a]

	(+36)GFP/(−)SiO_2	(+36)GFP/(+)3-APTMS	(−30)GFP/(+)3-APTMS	(−30)GFP/(−)SiO_2	(−7)GFP/(+)3-APTMS
k_{off} [s^{-1}]	6.90×10^{-2}		3.92×10^{-2}		1.01×10^{-1}
k_{on}* [s^{-1}]	4.60×10^{-3}		7.50×10^{-3}		2.50×10^{1}
F_{eq} [0-1]	0.17	0.97	0.12	0.98	0.78
C_{eq} [0-1]	0.83	0.03	0.88	0.02	0.22
C_{dark} [0-1]	0.20	0.04	0.19	0.06	0.14

[a]Molecule−post binding parameters for select interaction pairs determined by fitting experimental results to an analytical expression describing fluorescence recovery governed by binding.

regardless of charge.) For FRAP experiments involving eGFP and the positively charged post surface, protein−surface interactions clearly dictate the rate of the fluorescence recovery (Figure 7, green curve). For this pair, a bound fraction of 0.22 is obtained for C_{eq}, implying that a significant proportion of GFP molecules are interacting with the posts, consistent with the expected electrostatic interaction. This value is between that determined for the supercharged GFPs in like and oppositely charged surface environments (discussed below), consistent with the lower net charge (−7) on the eGFP molecule. Further evidence for electrostatic binding is seen in the values for C_{dark}. For a fixed surface coating of 3-APTMS, the steady-state dark fraction reduces from a value of 20% for the −30GFP to 14% for eGFP. This is consistent with the bound fraction being proportional to the magnitude of the electrostatic attraction. For eGFP in a positively charged surface environment, reaction with both the surface and hindered diffusion contributes to the recovery process; the release rate of $k_{off} = 0.101\ s^{-1}$ obtained from the simulation yields a characteristic recovery time of 1/0.1 = 10 s, which is on the order of the anticipated recovery time for diffusion $\Delta t = (d_{ROI}^2)/(4D_h) \sim 7$ s. These values imply that an eGFP molecule releases from the surface after ~10 s, which is on the order of the time required to diffuse through the region of interest. Therefore, both reaction and diffusion contribute to the observed fluorescence recovery rate.

For supercharged GFPs in environments where the post structures were of like charge to the diffusing species, similar diffusion coefficients were observed. $D_h = 25 \pm 2.4\ \mu m^2\ s^{-1}$ was determined for $d_{eff} = 388$ nm and a pitch of 500 nm and a $D_h = 36 \pm 0.3\ \mu m^2\ s^{-1}$ for a pitch of 700 nm. These values are the same, within error, as those obtained for eGFP and show an insensitivity of the GFP diffusion coefficient to charge repulsive environments. In these cases, diffusion of mobile species dominates the recovery process, with greater than 97% of the fluorescence recovery attributable to diffusion of mobile species back into the region of interest, as indicated by the values for F_{eq}. This is in sharp contrast to the opposite polarity, molecule−surface pairs. In these cases, only 17% of fluorescence recovery can be attributed to diffusion for the +36GFP/$-SiO_2$ pair and 12% for the −30GFP/+3-APTMS pair, respectively (Table 2). Thus, the bound fraction in these cases is much greater for surfaces and species with opposite polarity, consistent with the expected electrostatic interaction.

Complete fluorescence recovery to the prebleach intensity value was not achieved for oppositely charged protein−surface pairs. This is commonly attributed to a strong binding state, such as the electrostatic interaction expected here. Twenty percent of the total fluorescence (total concentration) is bound in this state for the (+36GFP/$-SiO_2$) pair and 19% for the (−30GFP/3-APTMS) pair (these values are listed as C_{dark} in Table 2). Fluorescence intensity recovery saturated at the level of steady-state fluorescence at ~70 and ~160 s, as measured from the termination of the photobleaching sequence, for the (+36GFP/$-SiO_2$) and (−30GFP/3-APTMS) binding pairs, respectively. In fact, fluorescence recovery remained at this relatively low steady-state recovery level for the maximum observation time of days, indicating that k_{off} approaches 0 for these interactions. This phenomenon can be attributed to bonding of charged GFP to the post surface that is bleached in place during the photobleaching phase of FRAP (or to bleached molecules that become immobilized). These bleached and strongly bound molecules fail to exchange with unbleached molecules during the recovery phase, thereby limiting the steady-state fluorescence recovery to a value below that of the prebleach phase. Therefore, the process of binding and release from the surface is too slow to effectively contribute to the recovery process.

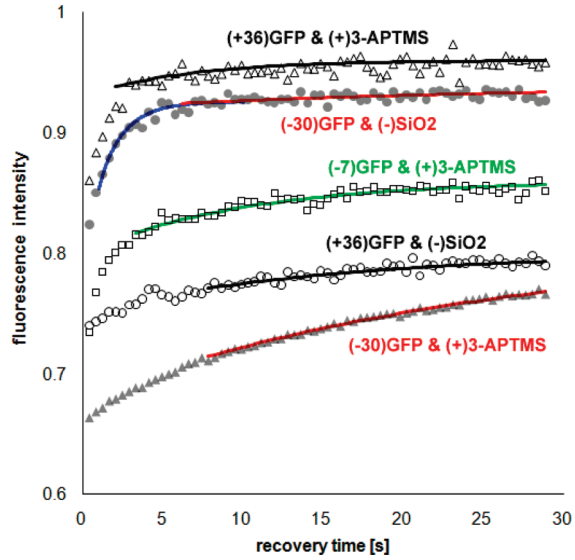

Figure 7. Experimental FRAP curves (data points) and analytical fits to the data points where the recovery was dictated by binding (solid lines). The superimposed blue line also shows an example of the best fit of simulation to the portion of the fluorescence recovery data dictated by molecular diffusion. The data represent the extreme cases of pure diffusion dominant behavior (for protein−surface pairs of matched polarity favoring dissolution) and reaction dominant behavior (for protein−surface pairs of opposite polarity favoring binding).

CONCLUSIONS

Advanced fabrication techniques facilitate the production of environments with defined surface areas and crowding elements. Arrays of high-density posts with diameters ranging from approximately 300 to 400 nm were fabricated and demonstrated to act as synthetic crowding elements that reduced the diffusive transport of engineered proteins and small fluorescent molecules. The diffusion coefficients of FITC and GFP

are reduced in these silicon post environments. This reduction is on the order of 60−70% when compared to the diffusion coefficient in dilute solution. This result indicates that the diffusion property can be manipulated over a significant range *via* synthetic crowding.

The effect of reactions with the surface of the post structures on diffusion of these species was also investigated. The posts could be chemically functionalized using a silane reagent to change the net surface charge of the posts. Supercharged variants of GFP provided a convenient means for examining the effect of electrostatic interactions on diffusive transport. The protein variants possessed significantly different net charges while maintaining other important physical properties, such as fluorescence characteristics and molecular weights, facilitating comparative analyses. These proteins were used to demonstrate that surface reactivity could be tuned to affect transport processes. When the time for molecular binding and release is on the same order as the time required for diffusive transport at the scale being examined, both reaction and diffusion contribute to species transport. This situation was observed for FRAP experiments involving eGFP in post array environments that were coated with an amine-terminated silane. In the extreme cases when the surface charges of the protein and post surface are alike or when the binding affinity is strong, the fluorescence recovery is primarily due to diffusion of the mobile element. In designing transport systems, such binding interaction rates are often unknown and can be difficult to characterize when surfaces are involved. The technique of FRAP combined with simulation provides a convenient means for interpreting values for binding and release rates and for hindered diffusion values. This information is valuable for the design of effective separation systems and microscale reaction systems and for interpreting the physical variables that affect cellular transport mechanisms.

METHODS

Device Fabrication. Post arrays integrated in microfluidic channels were created using a combination of electron beam and photolithographies along with cryogenic silicon etching. An overview of the fabrication process is shown in Figure 1. Electron beam lithography (EBL) was used to define the location and size of the post arrays. ZEP520A (ZEON Corporation, Tokyo, Japan) resist was coated on ⟨100⟩ silicon wafers at 6000 rpm for 45 s and baked at 180 °C for 2 min. Exposure was carried out in a JEOL JBX9300FS electron beam lithography system at an energy of 100 kV, and appropriate doses were chosen to achieve the desired post diameter. E-beam exposed wafers were developed in xylenes for 30 s, rinsed with isopropyl alcohol (IPA), and then dried with N_2 (Figure 1A).

After "descumming" samples for 6 s at 100 W in an oxygen plasma, a 15 nm thick film of Cr was deposited using a dual gun electron beam evaporation chamber (Thermionics, Port Townshend, WA). Conventional lift-off processing was performed to remove the majority of the Cr film, leaving Cr disks in the previously exposed regions of the sample (Figure 1B). These Cr patterns serve as a hard etch mask during cryogenic etching, ultimately defining the size and location of the post arrays.

Prior to etching, photolithography was used to define the microfluidic channels. Samples were precoated using an adhesion promoter and spin-coated with a negative tone photoresist, NFR016D255cP (JSR Micro Inc., Sunnyvale, CA), at 6000 rpm for 45 s. After soft baking at 90 °C for 90 s, the previously patterned nanopost features were aligned to the microchannel optical mask and exposed. A postexposure bake at 90 °C for 90 s was followed by development in MICROPOSIT MF CD-26 Developer (Shipley Company, Marlboro, MA) for approximately 20 s. After rinsing with DI water and drying with N_2, the wafer was baked on a hot plate at 180 °C for 3 min and was exposed to an oxygen plasma at 400 W for 30 s to remove any residual organic materials (Figure 1C).

A cryogenic silicon etching technique carried out in an Oxford Plasmalab 100 inductively coupled plasma reactive ion etching system was employed to simultaneously etch the microchannels and the posts. This process exposes samples to SF_6 and O_2 plasma at −110 °C. A flow rate of 18, 19, and 20 sccm of O_2 was introduced for 200, 100, and 50 nm nominal diameter posts, respectively. An etching time of 2 min provided approximately 6 μm of etch (Figure 1D).

The resist was stripped using a solution of 1165 at 70 °C for approximately 30 min. The wafers were washed and dried in a spin cleaner. Cr was removed by soaking the wafers in a Cr etchant for 3 min, followed by thorough rinsing with DI water and drying with N_2 (Figure 1E).

A plasma-enhanced chemical vapor deposition (PECVD, Oxford Plasmalab 100) technique was used for coating the structures with silicon dioxide. A 2 min process resulted in a coating of 50−60 nm on the side wall of vertical posts and 100−120 nm on surrounding horizontal surfaces. PECVD coating of silicon dioxide on post arrays increased the occupied volume of the post arrays, decreasing the gap distance between the posts. Scanning electron microscopy (SEM) images of the structures are shown in Figure 1I and were captured at $\theta = 15°$.

The net charge of the post array surface coated with silicon dioxide using PECVD is negative at neutral pH (Figure 1F).[40] In order to positively charge the post surfaces, the posts were functionalized with 3-aminopropyltrimethoxysilane (3-APTMS) by vapor deposition. Ten microliters of *N*,*N*-diisopropylethylamine and 30 μL of 3-APTMS were separately administered into a N_2-purged desiccator, and after 2 min of N_2 flow, the samples were left for 2 h.

Sample Preparation: Proteins and FITC. Enhanced green fluorescent protein (eGFP) and +36 and −30 supercharged GFPs were purified using a modification of a previously described method.[37] Briefly, the pDEST17-eGFP vector encoding the enhanced GFP tagged with 6x-His from a T7 promoter and the pET expression vectors encoding the supercharged GFPs were transformed into BL21(DE3)pLysS competent cells (Invitrogen). The transformed cells were grown to an optical density (OD) of 0.8 in 100 mL of Luria−Bertani (LB) broth media at 37 °C, and 1 mM IPTG (isopropyl-β-D-thiogalactopyranoside) was added to induce expression of the enhanced and the supercharged GFP proteins. Following 4−6 h of induction, the cells were collected by centrifugation and resuspended in lysis buffer (20 mM Tris-HCl, 1 M NaCl, and 5 mM imidazole; pH 7.5). Cells were lysed by sonication, and the 6x-His-tagged proteins were purified by HIS-Select nickel affinity gel (Sigma) according to the manufacturer's instructions. The purified proteins were exchanged into the final buffer (50 mM potassium phosphate buffer, 100 mM NaCl; pH 7.5) by using Amicon Ultra-15 centrifugal filter units (Millipore). The His-eGFP protein was diluted to a final concentration of 26.3 μM, and the final concentrations of the supercharged proteins were 20 μM for +36GFPs and 46 μM for −30GFPs, as estimated by absorbance at 280 nm (extinction coefficient = 17 330 M^{-1} cm^{-1}). Samples were further analyzed by sodium dodecyl sulfate−polyacrylamide gel electrophoresis (SDS−PAGE) (data not shown). The working solution of 200 μM FITC was prepared in 1 mM NaCl.

Preparation of Microfluidic Channel with Embedded Post Arrays. Transparent polydimethylsiloxane (PDMS, Sylgard 182 silicone elastomer base, Dow Corning) was used to seal the top of the microchannel device. Five milliliters of a 10:1 mixture of Sylgard 184 silicon base to curing agent was prepared in a Petri dish (100 mm). The mixture was degassed for approximately 15 min and then baked in an oven at 70 °C for approximately 1 h. After the baking process, it was cut into pieces in the shape of the chip, and two holes were created at the end of the channel for reagent reservoirs. After filling the channel, these holes were blocked with Valap in order to remove unintended flow that could interfere with the diffusion measurements.

FRAP Experiment. A Leica TCS SP2 scanning confocal microscope was employed to perform the FRAP experiments. This microscope is equipped with a 50 mW 488 nm Ar^+ laser, a long working distance dry objective (PL FL 63x/0.7, Leica), a tunable acousto-optical beam splitter (AOBS, Leica), and a dichroic mirror. Other parameters related to FRAP experiments are summarized as follows: 488 nm excitation wavelength, 495−600 nm emission wavelength, time-dependent *xy* scanning mode, 256 × 256 pixel scan, 4× magnification, frame acquisition time of 1 kHz, and bidirectional scanning. FRAP experiments were performed in "fly" mode and used 3, 5, and 70 image acquisitions for the prebleaching, bleaching, and postbleaching modes during FRAP, respectively. The bleached region-of-interest (ROI) was circular with dimensions of 15 μm diameter.

Simulation and Modeling. A reaction considering a single binding interaction was used to model the protein/post surface interaction for the purpose of simulation

$$F + S \leftrightarrow C \tag{1}$$

where *F*, *S*, and *C* are the concentrations of mobile protein, unoccupied binding sites, and bound protein, respectively. The nomenclature of the variables in eq 1 was selected in order to match that described by Sprague *et al.*[38] in their treatment on the analysis of binding reactions by FRAP. For the FRAP experiments reported here, both reaction dominant and pure diffusion dominant behaviors were observed. The treatment described by Sprague *et al.*[38] to model reaction dominant behavior was also implemented here, although a different Monte Carlo based particle tracking approach was used to simulate the pure diffusion dominant case. In the ensuing discussion, it is important to note that fluorescence intensity is directly proportional to concentration and thus

$$I(\mathrm{ROI}, t) = A_1 \times \frac{1}{xy}\int_x \int_y C_0(x, y, t)\mathrm{d}x\mathrm{d}y \tag{2}$$

indicating that the intensity at each time node during FRAP recovery is taken as the average concentration in a predefined ROI of dimensions *x* and *y*. Fluorescence recovery was reported with the intensity normalized to the prebleach, average intensity and thus *I*(ROI,*t*) fell within the range of (0−1).

Reaction Dominant Fluorescence Recovery. Purely reaction dominant fluorescence recovery behavior has been observed by Kaufman and Jain,[41] Bulinski *et al.*,[42] and Sprague *et al.*[38] in cellular scale environments and is represented by the following expression

$$I(t) = I_{max} - (I_{max} - I_{min})\mathrm{e}^{-k_{off}t} \tag{3}$$

where I_{max} is the maximum fluorescence intensity at full recovery, I_{min} is the intensity just after completion of photobleaching, and k_{off} is the off-rate for the binding interaction (the inverse of k_{off} is the mean residence time, in this case, of a bound protein on the functionalized Si post surface). It is important to note that eq 3 reduces to that reported as eq 11 in Sprague *et al.*[38] for reaction dominant behavior by dividing eq 3 by I_{max} and $C_{eq} = (I_{max} - I_{min})/I_{max}$.

C_{eq} is the concentration of bound molecules at equilibrium. All experiments reported in this work were conducted under C_{eq} conditions. It is important to note that even during the photobleaching and recovery phases of FRAP that C_{eq} remains constant but partitioned between (bound/bleached) and (bound/unbleached) molecules

$$C_{eq} = C_{bleached} + C_{unbleached} = \frac{k_{on}^*}{k_{on}^* + k_{off}} \tag{4}$$

k_{on}^* is an effective on-rate describing the protein/post interaction and is used in place of k_{on} under circumstances where the binding site concentration (S_{eq}) is unknown (*i.e.*, $k_{on}^* = k_{on} \times S_{eq}$).[38] This is the convention used here considering that the number of binding sites on the SiO_2 and 3-APTMS-coated post surfaces were unknown. F_{eq} represents the equilibrium concentration of mobile protein.

The best fit to eq 3 to the recovery data was used to extrapolate back to $t = 0$ s, the termination of photobleaching, in order to determine the fraction of fluorescence due to bound (C_{eq}), and unbound (F_{eq}) molecules within the bleach ROI. This was determined by modulating I_{max}, I_{min}, and k_{off} and implementing the sum-of-the-squares fitting method to determine the best fit solution. In addition, the data range for the fitting procedure was also modulated during the data fitting process (t_o:Δ*t*:t_f, t_1:Δ*t*:t_f, *etc.*). This procedure acted to exclude the initial acquisition steps, data that included primarily diffusion-based information where mobile and bleached molecules rapidly existed within the ROI. Indeed, it was found that the best fit solutions always excluded the initial data points.

Pure Diffusion Dominant Behavior. A particle tracking method was used to simulate the diffusion of a collection of point particles representing virtual GFP and FITC molecules in a virtual post environment. The simulation best emulated real experiments by importing scanning electron microscope images of actual post arrays into the simulation environment. Further details of the simulation technique are provided in the Supporting Information. Figure S1 shows the predicted change in the diffusion coefficient as a function of time by simulation for the diffusion of eGFP in an environment consisting of a 2D hexagonal array of posts. This figure illustrates why the time-independent hindered diffusion coefficient is anticipated to affect fluorescence recovery during the acquisition time of photobleaching experiments reported in this work. Briefly, an initial guess is made for the time-independent diffusion coefficient of the molecule of interest (D_o) and the simulation is initiated. As the walk progresses, the volume occupied by the post rapidly reduces the value of D_o to a lower steady-state value of D_h. The actual value of the diffusion coefficient is derived from the simulation for four specific directions in the *xy* plane including D_{xx}, D_{yy}, D_{xy}, and D_{yx}. However, little difference in magnitude between these values was observed for the post arrays reported here due to the hexagonal symmetry of the posts and the large size of the photobleached ROI relative to the post pitch. Thus, D_h is reported for the purpose of brevity and is computed as a simple average of the four derived *D* values. However, in the finite differencing simulation described next, the D_{xx}, D_{yy}, D_{xy}, and D_{yx} values were used for input.

A finite differencing scheme emulating fluorescence recovery by solving the time-dependent parabolic diffusion equation was then executed using the values D_{xx}, D_{yy}, D_{xy}, and D_{yx}. Simulated fluorescence recovery accurately predicted the experimental data for the cases of pure diffusion, and as a result, the reported values of D_o and D_h were taken as representative of the experimental system. Since D_o for GFP has been measured previously, the refined value of D_o provided a control for comparison with the known value. D_o has been reported in the literature as 87 μm^2 s^{-1} for GFP[43] and 260 μm^2 s^{-1} for FITC.[44,45]

The time-dependent, parabolic diffusion equation was solved by the explicit finite differencing numerical scheme to simulate FRAP. The form of the equation was

$$\frac{\partial C(x,y,t)}{\partial t} = D_{xx}(x,y,t)\frac{\partial^2 C(x,y,t)}{\partial x^2} + D_{yy}(x,y,t)\frac{\partial^2 C(x,y,t)}{\partial y^2} + (D_{xy}(x,y,t) + D_{yx}(x,y,t))\frac{\partial^2 C(x,y,t)}{\partial x \partial y} \tag{5}$$

where *C* represents the concentration of unbleached fluorophore in the ROI as a function of space and time. $C(x,y,t = 0)$

was set to equal the unbleached fraction observed for each experiment (C_o) and $C(x = x_{max}, y = y_{max}, t) = 1$ owing to the significant pool of unbleached GFP surrounding the post array.

Acknowledgment. We thank D. R. Liu (HHMI, Harvard University) for the generous gift of supercharged GFP expression vectors. This research was supported by NIH Grant EB000657. A portion of this research (device fabrication) was conducted at the Center for Nanophase Materials Sciences, which is sponsored at Oak Ridge National Laboratory by the Division of Scientific User Facilities, U.S. Department of Energy. This work was performed at the Oak Ridge National Laboratory, managed by UT-Battelle, LLC, for the U.S. DOE under Contract No. DE-AC05-00OR22725.

Supporting Information Available: Results of a Monte Carlo, random walk simulation and scanning electron microscopic images verifying post pitch. This material is available free of charge *via* the Internet at http://pubs.acs.org.

REFERENCES AND NOTES

1. Hall, D.; Minton, A. P. Macromolecular Crowding: Qualitative and Semiquantitative Successes, Quantitative Challenges. *Biochim. Biophys. Acta* **2003**, *1649*, 127–139.
2. Ellis, R. J. Macromolecular Crowding: Obvious but Underappreciated. *Trends Biochem. Sci.* **2001**, *26*, 597–604.
3. Derenyi, I.; Astumian, R. D. AC Separation of Particles by Biased Brownian Motion in a Two-Dimensional Sieve. *Phys. Rev. E* **1998**, *58*, 7781–7784.
4. Astumian, R. D. Generalized Fluctuation−Dissipation and Reciprocal Relations for Brownian Sieves and Molecular Machines. *Phys. Rev. E* **2009**, *79*, 021119–021115.
5. Earhart, C. M.; Wilson, R. J.; White, R. L.; Pourmand, N.; Wang, S. X. Microfabricated Magnetic Sifter for High-Throughput and High-Gradient Magnetic Separation. *J. Magn. Magn. Mater.* **2009**, *321*, 1436–1439.
6. Conlisk, A. T.; McFerran, J.; Zheng, Z.; Hansford, D. Mass Transfer and Flow in Electrically Charged Micro- and Nanochannels. *Anal. Chem.* **2002**, *74*, 2139–2150.
7. Zheng, Z.; Hansford, D. J.; Conlisk, A. T. Effect of Multivalent Ions on Electroosmotic Flow in Micro- and Nanochannels. *Electrophoresis* **2003**, *24*, 3006–3017.
8. Adiga, S. P.; Jin, C.; Curtiss, L. A.; Monteiro-Riviere, N. A.; Narayan, R. J. Nanoporous Membranes for Medical and Biological Applications. *Wiley Interdisciplinary Reviews: Nanomedicine and Nanobiotechnology* **2009**, *1*, 568–581.
9. Ai, B.-q. Transport of Overdamped Brownian Particles in a Two-Dimensional Tube: Nonadiabatic Regime. *Phys. Rev. E* **2009**, *80*, 011113–011114.
10. Chou, C.-F.; Bakajin, O.; Turner, S. W. P.; Duke, T. A. J.; Chan, S. S.; Cox, E. C.; Craighead, H. G.; Austin, R. H. Sorting by Diffusion: An Asymmetric Obstacle Course for Continuous Molecular Separation. *Proc. Natl. Acad. Sci. U.S.A.* **1999**, *96*, 13762–13765.
11. Doktycz, M. J.; Simpson, M. L. Nano-Enabled Synthetic Biology. *Mol. Syst. Biol.* **2007**, 3.
12. Long, M. S.; Jones, C. D.; Helfrich, M. R.; Mangeney-Slavin, L. K.; Keating, C. D. Dynamic Microcompartmentation in Synthetic Cells. *Proc. Natl. Acad. Sci. U.S.A.* **2005**, *102*, 5920–5925.
13. Pielak, G. J. A Model of Intracellular Organization. *Proc. Natl. Acad. Sci. U.S.A.* **2005**, *102*, 5901–5902.
14. Ayres, S., Jr. Autoimmune Diseases: Cell Membrane Protection *vs.* Immunosuppression. *Int. J. Dermatol.* **1983**, *22*, 333–334.
15. Porat, A.; Elazar, Z. Regulation of Intra-Golgi Membrane Transport by Calcium. *J. Biol. Chem.* **2000**, *275*, 29233–29237.
16. Bader, R.; Herzog, K.; Kao, W. A Study of Diffusion in Poly(ethyleneglycol)-Gelatin Based Semi-interpenetrating Networks for Use in Wound Healing. *Polym. Bull. (Berlin)* **2009**, *62*, 381–389.
17. Fowlkes, J. D.; Fletcher, B. L.; Hullander, E. D.; Klein, K. L.; Hensley, D. K.; Melechko, A. V.; Simpson, M. L.; Doktycz, M. J. Tailored Transport through Vertically Aligned Carbon Nanofibre Membranes; Controlled Synthesis, Modelling, and Passive Diffusion Experiments. *Nanotechnology* **2005**, *16*, 3101–3109.
18. Remaley, A. T.; *et al.* Synthetic Amphipathic Helical Peptides Promote Lipid Efflux from Cells by an Abca1-Dependent and an Abca1-Independent Pathway. *J. Lipid Res.* **2003**, *44*, 828–836.
19. Retterer, S. T.; Siuti, P.; Choi, C. K.; Thomas, D. K.; Doktycz, M. J. Development and Fabrication of Nanoporous Silicon-Based Bioreactors within a Microfluidic Chip. *Lab Chip* **2010**, *10*, 1174–1181.
20. Mitchell, D. T.; Lee, S. B.; Trofin, L. C. M.; Li, N.; Nevanen, T. K.; Soderlund, H.; Martin, C. R. Smart Nanotubes for Bioseparations and Biocatalysis. *J. Am. Chem. Soc.* **2002**, *124*, 11864–11865.
21. Fletcher, B. L.; McKnight, T. E.; Fowlkes, J. D.; Allison, D. P.; Simpson, M. L.; Doktycz, M. J. Controlling the Dimensions of Carbon Nanofiber Structures through the Electropolymerization of Pyrrole. *Synth. Met.* **2007**, *157*, 282–289.
22. Fletcher, B. L.; Retterer, S. T.; McKnight, T. E.; Melechko, A. V.; Fowlkes, J. D.; Simpson, M. L.; Doktycz, M. J. Actuatable Membranes Based on Polypyrrole-Coated Vertically Aligned Carbon Nanofibers. *ACS Nano* **2008**, *2*, 247–254.
23. Kececi, K.; Sexton, L. T.; Buyukserin, F.; Martin, C. R. Resistive-Pulse Detection of Short Dsdnas Using a Chemically Functionalized Conical Nanopore Sensor. *Nanomedicine* **2008**, *3*, 787–796.
24. Oh, K. W.; Ahn, C. H. A Review of Microvalves. *J. Micromech. Microeng.* **2006**, *16*, R13–R39.
25. Kumar, A.; Srivastava, A.; Galaev, I. Y.; Mattiasson, B. Smart Polymers: Physical Forms and Bioengineering Applications. *Prog. Polym. Sci.* **2007**, *32*, 1205–1237.
26. Hess, B.; Mikhailov, A. Microscopic Self-Organization in Living Cells: A Study of Time Matching. *J. Theor. Biol.* **1995**, *176*, 181–184.
27. Misteli, T. The Concept of Self-Organization in Cellular Architecture. *J. Cell Biol.* **2001**, *155*, 181–185.
28. Choi, C. K.; Margraves, C. H.; Kihm, K. D. Examination of Near-Wall Hindered Brownian Diffusion of Nanoparticles: Experimental Comparison to Theories by Brenner (1961) and Goldman *et al.* (1967). *Phys. Fluids* **2007**, 19.
29. Banks, D. S.; Fradin, C. Anomalous Diffusion of Proteins Due to Molecular Crowding. *Biophys. J.* **2005**, *89*, 2960–2971.
30. Garcia-Perez, A. I.; López-Beltrán, E. A.; Klúner, P.; Luque, J.; Ballesteros, P.; Cerd, S. Molecular Crowding and Viscosity as Determinants of Translational Diffusion of Metabolites in Subcellular Organelles. *Arch. Biochem. Biophys.* **1999**, *362*, 329–338.
31. Guigas, G.; Kalla, C.; Weiss, M. Probing the Nanoscale Viscoelasticity of Intracellular Fluids in Living Cells. *Biophys. J.* **2007**, *93*, 316–323.
32. Weiss, M.; Elsner, M.; Kartberg, F.; Nilsson, T. Anomalous Subdiffusion Is a Measure for Cytoplasmic Crowding in Living Cells. *Biophys. J.* **2004**, *87*, 3518–3524.
33. Sanabria, H.; Kubota, Y.; Waxham, M. N. Multiple Diffusion Mechanisms Due to Nanostructuring in Crowded Environments. *Biophys. J.* **2007**, *92*, 313–322.
34. Fowlkes, J. D.; Fletcher, B. L.; Retterer, S. T.; Melechko, A. V.; Simpson, M. L.; Doktycz, M. J. Size-Selectivity and Anomalous Subdiffusion of Nanoparticles through Carbon Nanofiber-Based Membranes. *Nanotechnology* **2008**, *19*, 415301.
35. Fowlkes, J. D.; Hullander, E. D.; Fletcher, B. L.; Retterer, S. T.; Melechko, A. V.; Hensley, D. K.; Simpson, M. L.; Doktycz, M. J. Molecular Transport in a Crowded Volume Created from Vertically Aligned Carbon Nanofibres: A Fluorescence Recovery after Photobleaching Study. *Nanotechnology* **2006**, *17*, 5659–5668.
36. Spitzer, J.; Poolman, B. The Role of Biomacromolecular Crowding, Ionic Strength, and Physicochemical Gradients in the Complexities of Life's Emergence. *Microbiol. Mol. Biol. Rev.* **2009**, *73*, 371–388.

37. Lawrence, M. S.; Phillips, K. J.; Liu, D. R. Supercharging Proteins Can Impart Unusual Resilience. *J. Am. Chem. Soc.* **2007**, *129*, 10110–10112.
38. Sprague, B. L.; Pego, R. L.; Stavreva, D. A.; McNally, J. G. Analysis of Binding Reactions by Fluorescence Recovery after Photobleaching. *Biophys. J.* **2004**, *86*, 3473–3495.
39. Elowitz, M. B.; Surette, M. G.; Wolf, P.-E.; Stock, J. B.; Leibler, S. Protein Mobility in the Cytoplasm of *Escherichia coli*. *J. Bacteriol.* **1999**, *181*, 197–203.
40. Boogaard, A.; Kovalgin, A. Y.; Wolters, R. A. M. Net Negative Charge in Low-Temperature SiO_2 Gate Dielectric Layers. *Microelectron. Eng.* **2009**, *86*, 1707−1710.
41. Kaufman, E. N.; Jain, R. K. Measurement of Mass Transport and Reaction Parameters in Bulk Solution Using Photobleaching. Reaction Limited Binding Regime. *Biophys. J.* **1991**, *60*, 596–610.
42. Bulinski, J. C.; Odde, D. J.; Howell, B. J.; Salmon, T. D.; Waterman-Storer, C. M. Rapid Dynamics of the Microtubule Binding of Ensconsin *In Vivo*. *J. Cell Sci.* **2001**, *114*, 3885–3897.
43. Potma, E. O.; de Boeij, W. P.; Bosgraaf, L.; Roelofs, J.; van Haastert, P. J. M.; Wiersma, D. A. Reduced Protein Diffusion Rate by Cytoskeleton in Vegetative and Polarized Dictyostelium Cells. *J. Cell Sci.* **2001**, *81*, 2010−2019.
44. Periasamy, N.; Verkman, A. S. Analysis of Fluorophore Diffusion by Continuous Distributions of Diffusion Coefficients: Application to Photobleaching Measurements of Multicomponent and Anomalous Diffusion. *Biophys. J.* **1998**, *75*, 557–567.
45. Seksek, O.; Biwersi, J.; Verkman, A. S. Translational Diffusion of Macromolecule-Sized Solutes in Cytoplasm and Nucleus. *J. Cell Biol.* **1997**, *138*, 131–142.